GSI

GSI-94-36
PREPRINT
JUNI 1994

MULTIFRAGMENTATION OF SPECTATORS IN RELATIVISTIC HEAVY-ION REACTIONS

A.S. BOTVINA, I.N. MISHUSTIN et al.

Gesellschaft für Schwerionenforschung mbH
Postfach 110552 · D-64220 Darmstadt · Germany

Multifragmentation of Spectators in Relativistic Heavy-Ion Reactions

A.S. Botvina[a,§] and I.N. Mishustin[b]

[a] *Institute for Nuclear Research, Russian Academy of Sciences, 117312 Moscow , Russia*

[b] *Kurchatov Institute, Russian Scientific Center, 123182 Moscow , Russia*

and

M. Begemann-Blaich,[c] J. Hubele,[d] G. Imme,[e] I. Iori,[f] P. Kreutz,[c] G.J. Kunde,[d,†] W.D. Kunze,[d] V. Lindenstruth,[d,‡] U. Lynen,[d] A. Moroni,[f] W.F.J. Müller,[d] C.A. Ogilvie,[d,#] J. Pochodzalla,[d] G. Raciti,[e] Th. Rubehn,[d] H. Sann,[d] A. Schüttauf,[c] W. Seidel,[g] W. Trautmann,[d] and A. Wörner[d]

[c] *Institut für Kernphysik, Universität Frankfurt, D-60486 Frankfurt, Germany*

[d] *Gesellschaft für Schwerionenforschung, D-64220 Darmstadt, Germany*

[e] *Dipartimento di Fisica dell' Universitá and I.N.F.N., I-95129 Catania, Italy*

[f] *Instituto di Scienze Fisiche, Universita degli Studi di Milano and I.N.F.N., I-20133 Milano, Italy*

[g] *Forschungszentrum Rossendorf, D-01314 Dresden, Germany*

[§] *Present address: Hahn-Meitner Institut, D-14109 Berlin, Germany*

[†] *Present address: National Superconducting Cyclotron Laboratory, MSU, East Lansing, MI 48824, USA*

[‡] *Present address: Nuclear Science Division, LBL, Berkeley, CA 94720, USA*

[#] *Present address: Department of Physics, MIT, Cambridge, MA 02139, USA*

ABSTRACT

Using the ALADIN forward-spectrometer at SIS we have studied multi-fragment decays of ^{197}Au projectiles after collisions with C, Al, Cu, and Pb targets at a bombarding energy of $E/A = 600$ MeV. The new data presented in this work comprise the measured cross sections of multi-fragment processes, the N/Z ratios of the produced fragments, and the differential distributions of fragment multiplicities and of observables built on the charge correlations within the event.

The ^{197}Au + Cu data are analyzed with the Statistical Multifragmentation Model. It is shown that all observables can be simultaneously reproduced on an absolute scale, apart from an overall normalization constant which relates the number of model events to the measured cross section. A continuous distribution of excited residual nuclei, used as input for the calculations, was derived from the criterion of a best fit to the data. It exhibits a correlation between decreasing mass number A with increasing excitation energy E_x/A and a saturation of the excitation energy at $E_x/A \approx 8$ MeV.

NUCLEAR REACTIONS

C, Al, Cu, Pb(^{197}Au,X), $E/A = 600$ MeV; measured fragment cross sections, fragment charge and mass, charge asymmetries; analysis with Statistical Multifragmentation Model.

1 Introduction

Presently the phenomenon of multiple fragment production in nuclear reactions is widely investigated in many laboratories [1, 2]. The large interest in these studies is explained by the rich physics associated with the formation and break-up of highly excited nuclear systems. It is possible to look at the multifragmentation phenomenon in different ways. Firstly, it may be used to obtain information about nuclei under the extreme conditions of high excitation energy, high angular momentum, and of collective flow. Secondly, by analysing the reaction products one may study the reaction mechanism and, in particular, the nonequilibrium stage of the reaction. And finally, the multifragmentation phenomenon may be treated as a manifestation of the "liquid-gas" phase transition in a finite nuclear system. Very different multifragmentation models exist at present, a fact which reflects the diversity of this phenomenon.

The obvious success of the statistical models in describing the yields of intermediate-mass fragments indicates that a certain state of thermodynamic equilibrium is established during the later stages of the reaction [2-9]. In this work we will focus on the characteristics of the ensemble of excited nuclei formed at this time in the reaction process. In particular, we will address the question what maximum excitation energy can be absorbed by a thermalized nucleus.

We believe that there are two ways of "preparing" an intermediate nuclear system which can evolve to the complete break-up into fragments and light particles. The first way is associated with hadron-nucleus reactions and peripheral nucleus-nucleus collisions at high energies. In this case one can expect the formation of thermalized residual nuclei which undergo a statistical break-up. The second way is associated with head-on collisions of heavy nuclei at intermediate energies. At the initial stage of such collisions the nuclear matter may be compressed and heated-up at the same time. If the excitation energy is not too high, fragments may be formed at the expansion stage by a condensation or coalescence mechanism. In reality these two modes of fragment production may coexist and gradually replace one another with changing impact parameter and bombarding energy.

The aim of this paper is to investigate the multifragmentation in peripheral nuclear

collisions where one would expect the predominantly statistical break-up. We will consider the reactions of ^{197}Au on C, Al, Cu, and Pb targets at $E/A = 600$ MeV which were studied with the ALADIN spectrometer at SIS [8-11]. Analyses of these data [8, 9, 12, 13] have shown that the process of the peripheral-type collisions can be divided into three stages:

1) the fast dynamical stage dominated by the "hard" collisions of projectile and target nucleons,

2) the formation of highly-excited thermalized nuclear systems (TNS) from the spectator parts of the colliding nuclei, and

3) the statistical break-up of the TNS.

The properties of the formed residual nuclei or TNS were extracted from an analysis of the measured correlations of the fragment charges [9] with statistical multifragmentation models [12-14]. Several groups were able to show that not only the mean number of intermediate-mass fragments but also the mean values of other charge correlations, such as the relative asymmetries between the atomic numbers of the heaviest fragments and higher-order charge correlations, can be reproduced simultaneously and to high accuracy. This was achieved by adjusting the initial TNS masses and excitation energies. According to these analyses, the TNS distributions are characterized by a correlation of decreasing TNS mass number A with increasing excitation energy per nucleon E_x/A and by a saturation of the excitation energy at values between $E_x/A \approx 6$ to 8 MeV

The new analysis of the ALADIN data, presented in this paper, is based on additional experimental observables and is motivated by the following reasons:

a) In the previous work only average (integrated) observables have been described. Here we will present differential distributions which carry more detailed information about the multifragmentation process.

b) In the previous analyses a limited set of thermalized nuclei with given values for the mass A, atomic number Z, and excitation energy E_x has been considered to simulate the fragmentation sources. In reality, a rather broad and continuous distribution of TNS in mass and excitation energy should be expected. We will construct this distribution for the ^{197}Au + Cu reaction from the criterion of a best fit to the data. The experimental constraints will include the measured distribution of the fragmentation cross section which

will be reproduced up to an overall normalization constant.

c) The sequential decay of excited fragments affects the observed fragmentation patterns. A realistic treatment of this last reaction step is therefore indispensable. We will test this part of the model by comparing the calculated and measured N/Z distributions of the fragments.

d) The charge correlations presented in [9] were generated with a threshold set at fragment charges $Z \geq 2$. This includes alpha particles which may come from several sources and which are partly emitted into regions of momentum space outside the acceptance of the ALADIN spectrometer. This introduces a particular uncertainty for the model comparison, even though secondary decays are considered. We will therefore present the data and the theoretical results with a lower threshold of $Z \geq 3$ which is applied to all observables.

2 Experimental details and results

The experiment was performed with the ALADIN spectrometer at SIS [11]. Beams of ^{197}Au with an incident energy $E/A = 600$ MeV were directed onto targets of C, Al, Cu, and Pb with areal densities corresponding to interaction probabilities between $\approx 1\%$ and 3%.

The acceptance of the spectrometer and the coverage of solid angle by the detectors were sufficient to detect close to 100% of the heavier fragments originating from the decay of the projectile spectator. For the lighter fragments, the acceptance was estimated to be of the order of 1.0 - 2·exp(-Z) where Z is the fragment atomic number [8]. For lithium nuclei, the smallest fragments considered here, this corresponds to losses of the order of 10%. Other uncertainties, originating from misidentification of fragments and from non-resolved double hits, are expected to be of a comparable magnitude. It represents the level of accuracy up to which the present analysis can be carried out. No corrections for these effects were applied to the data, and neither to the results of the calculations.

The charge and multiplicity of nuclear fragments were determined by means of the time-of-flight (TOF) wall, located at the end of the ALADIN spectrometer. The discriminator threshold was set to be below $Z = 2$ particles. Elements with $Z \leq 8$ were resolved

individually by measuring the energy loss in the TOF-wall detectors. For heavier fragments the resolution assumed values of $\Delta Z \approx 4$ (FWHM). The TP-MUSIC detector, capable of resolving the individual elements for $Z \geq 8$, was used to calibrate the charge response of the TOF wall.

Light particles, predominantly originating from the mid-rapidity source, were detected by the 64 elements of a Si-CsI(Tl) hodoscope with a solid-angle coverage of approximately 50% between angles $\theta_{lab} = 7°$ and 25° and 15% between $\theta_{lab} = 25°$ and 40°. A minimum multiplicity of one particle in the target hodoscope was required in the off-line analysis. The on-line trigger condition was a beam particle in the start detector, placed upstream from the target, and no fragment larger than $Z \approx 70$ in the central part of the TOF wall. This trigger condition and the minimum hodoscope multiplicity of one should be met by all interactions occurring in the target except for the most peripheral collisions. Scaled-down beam events were recorded for the measurement of the beam-intensity.

The quantity Z_{bound} has been found very useful for a classification of the observed fragmentation events [8, 9, 11]. Z_{bound} is defined as the sum of all projectile fragments with $Z \geq 2$ that are detected with the TOF wall. With a threshold set at $Z \geq 3$ the analogous quantity Z_{b3} may be defined as the sum over all fragments with $Z \geq 3$. The target independence observed for the charge correlations as a function of Z_{bound} will be shown to hold for Z_{b3} equally well (section 4). In fig. 1 we show the mean number of $Z = 2$ particles as a function of Z_{bound} for the four target cases. It reaches values of about 3 for $Z_{bound} \approx 20$ to 50. Accordingly, Z_{bound} and Z_{b3} differ by about 6 units in this region, on average. The differences are smaller at lower and higher Z_{bound}. Note also the target independence of the measured helium multiplicities.

Absolute cross sections were determined by normalizing the measured event rate with respect to the thickness of the target and the rate of incoming beam particles. In fig. 2 the differential cross sections $d\sigma/dZ_{bound}$ (top) and $d\sigma/dZ_{b3}$ (bottom) are shown for the four reactions. The displayed integrated cross sections amount to 1.9 b, 2.4 b, 3.6 b, and 6.6 b for the C, Al, Cu, and Pb targets, respectively. At $Z_{bound}(Z_{b3})$ close to $Z_{beam} = 79$ the measured yields are dominated by the cutoff caused by the experimental trigger. The cross sections of the peripheral collisions in the range of $Z_{bound}(Z_{b3})$ around 50 to 60 depend

weakly on the target A as one would expect. The target dependence becomes dramatic for the more violent events at smaller $Z_{bound}(Z_{b3})$; the probability that in central collisions only a small number of $Z \geq 2$ (or $Z \geq 3$) fragments survive grows rapidly with increasing mass of the target. The impact parameter dependence of the multi-fragment channels [11] is also evident from the figure. The largest fragment multiplicities are observed for $Z_{bound} \approx 40$, i.e. for the most central collisions with the C target and for increasingly more peripheral collisions with the heavier targets. Note that the structures seen at small $Z_{bound}(Z_{b3})$ only reflect the thresholds $Z \geq 2(3)$ chosen for the summation of the fragment charges. For the Pb target, the first two channels are out of the ordinate range chosen for the figures; the cross sections of these channels are given in the figure caption.

The magnetic rigidity of the detected projectile fragments was determined by measuring their trajectories with the TP-MUSIC detector located between the magnet and the TOF wall. Combined with the charge information from the TP-MUSIC detector, obtained with a resolution $\Delta Z = 0.5$ (FWHM), and with the fragment time-of-flight (resolution $\Delta t/t \approx 1\%$) it yields the fragment mass [15]. The obtained resolution was $\Delta A/A \approx 3\%$ (FWHM). Individual masses of the lighter fragments, above the detection threshold $Z \geq 8$ of the TP-MUSIC, were thus resolved. In fig. 3 we show the measured ratios $N/Z = (A-Z)/Z$ (top) and the mean values of this quantity (bottom) as a function of Z for fragments from the reaction on the Cu target. The scatter plot representation illustrates the charge resolution achieved with the TP-MUSIC detector. The group of beam particles at $Z = 79$ results from scaled-down events. The produced fragments are on the neutron poor side of the valley of stability (long-dashed line) and follow to a good approximation the empirical EPAX parameterization [16]. The mean $\langle N/Z \rangle$ ratios are well reproduced by the calculations described in the following section.

Differential representations of some of the measured charge and multiplicity distributions have already been reported [9-11], mostly in the form of scatter plots which give qualitative impressions of the measured distribution widths. In section 4 we will present complete sets of the measured distributions for the multiplicity M_{imf} of intermediate-mass fragments ($3 \leq Z \leq 30$), for Z_{b3}, for the atomic number Z_{max} of the largest fragment of an event, and for the charge asymmetries A_{12} and A_{23} between the two largest fragments

and between the second and third largest fragment (figs. 8-13). The data are sorted either according to M_{imf} or into finite bins of Z_{b3}. The data will be compared to the results of the calculations described in the next section.

3 Model description

In our calculations we use the statistical multifragmentation model (SMM) developed in refs. [3, 4, 17]. Within the SMM we consider a microcanonical ensemble of all break-up channels composed of nucleons and excited fragments of different masses. It is assumed that an excited nucleus expands to a certain volume and then breaks up into nucleons and hot fragments. All possible break-up channels are considered. It is also assumed that at the break-up time the nucleus is in thermal equilibrium characterized by the channel temperature T determined from the energy balance. The probability W_j of a decay channel j is proportional to its statistical weight:

$$W_j \sim exp\ S_j(E_x, A, Z), \tag{1}$$

where S_j is the entropy of the system in a state corresponding to the decay channel j. The excitation energy, mass, and charge of the decaying system are denoted by E_x, A, and Z, respectively. The fragments with mass number $A_f > 4$ are treated as heated nuclear liquid drops. Each fragment contributes the bulk-, surface-, Coulomb-, and translational terms to the free energy and to the entropy of the system. The light fragments with $A_f \leq 4$ are considered as elementary particles ("nuclear gas"), having only translational degrees of freedom. The Coulomb interaction between all fragments and gas particles is taken into account via the Wigner-Seitz approximation. The surface tension of droplets is parameterized in such a way that it vanishes at a critical temperature $T_c = 18$ MeV corresponding to the "liquid-gas" phase transition.

The break-up channels are simulated by the Monte-Carlo method according to their statistical weights. In the present calculations it was assumed that the break-up occurs at a density of one third of the normal nuclear density ρ_0. This value appears preferable for the disintegration of spectator nuclei for which a compression and subsequent expansion, expected for central collisions of heavy nuclei and possibly leading to smaller densities, seems

unlikely. After break-up of the system the fragments propagate independently in their mutual Coulomb fields and undergo secondary decays. The deexcitation of large fragments ($A_f > 16$) is described by the evaporation-fission model, and for smaller fragments by the Fermi break-up model (see refs. [3, 18]). The correct description of the secondary decays is especially important for very large primary fragments which contribute considerably to the intermediate-mass fragment production at moderate excitation energies $E_x/A \approx 2$ to 4 MeV. We have therefore checked our evaporation, fission, and Fermi break-up models for nuclear reactions at low and intermediate energies. The isotopic composition of the detected reaction products reflects these final decay steps. Figure 3 shows that the calculated average neutron-to-proton ratios $\langle N/Z \rangle$ compare well with the measured result.

The most difficult part of this analysis is in selecting the TNS ensemble produced after the nonequilibrium stage of the reaction. Unfortunately, the present dynamical models are incapable of unambiguous predictions (see refs. [12, 13]). There is the possibility, however, to extract the TNS distribution from the experimental data. The previous comparisons of the statistical multifragmentation models with the integrated data allowed one to find a general correlation between mean mass $\bar{A}$ and excitation energy E_x of the residual nuclei [12-14]. Figure 4 shows the obtained distributions of TNS's. They were derived from the requirement of a best description of the mean multiplicities and the mean values of other charge correlations characterizing the emission of intermediate-mass fragments. In this work we go beyond that analysis by considering TNS ensembles which are continuous in A and E_x. We assume Gaussian distributions of A around the mean values $\bar{A}$. These mean values are related with the excitation energy per nucleon $\epsilon = E_x/A$ by the formula:

$$\alpha \equiv \frac{\bar{A}}{A_0} = 1 - 0.001 \cdot \epsilon - 0.015 \cdot \epsilon^2, \tag{2}$$

where ϵ is in MeV. This curve gives a good representation of the results of refs. [12-14] as shown in fig. 4.

The linear term in eq.(2) is actually quite small and not essential. This is quite different from the correlations calculated in the framework of the intranuclear cascade model [4, 12]. The cascade calculations predict a nearly linear dependence of the initially deposited energy on the number of lost nucleons and do not predict a saturation. The present analysis

provides some indications for a limitation of the excitation energy of hot residual nuclei, apparently resulting from prequilibrium emission. If an initially large energy is transferred to the residual nucleus, a correspondingly large fraction of it will be carried away by fast particles prior to the break-up. One may expect that the excitation energy comparable with the binding energy of fragments could be the natural limit. Equation (2) implies a maximum excitation energy $\epsilon_{max} = E_{max}/A = 8.13$ MeV (a formal solution at $\alpha \rightarrow 0$). The formula also reflects a natural correlation between the excitation energy and the mass number of a residual nuclear system formed after the nonequilibrium stage of the reaction: the more particles that are removed, the higher the excitation energy (per nucleon) that is achieved in the remnant.

The widths of the TNS mass distributions around the mean values $\bar{A}$ are parameterized as

$$\sigma = \sigma_0 \cdot (1 + c_0 \cdot \frac{\epsilon^2}{\epsilon^2_{max}}). \tag{3}$$

The coefficients σ_0 and c_0 are chosen to reproduce the widths of the experimental multiplicity distributions of intermediate-mass fragments. The increase of the width with the excitation energy (as illustrated by the vertical "error" bars in fig. 4) is compatible with the stochastic nature of the TNS formation process. The atomic numbers Z of the TNS ensemble were derived from the masses by applying the ratio $Z/A = 0.40$ of the ^{197}Au projectiles.

The relative yields $Y(\epsilon)$ of residues with different energy $\epsilon = E_x/A$ are determined entirely by the initial stage of the reaction. We choose a reasonable parameterization for the yields that leads to a good description of the observables. Our analysis showed that the functional form of $Y(\epsilon)$ is not at all trivial. At low energy $\epsilon \leq \epsilon_1$ it can be chosen in a simple exponential form:

$$Y(\epsilon) \sim exp(-c_1 \frac{\epsilon}{\epsilon_{max}}). \tag{4}$$

In fact, this kind of behaviour is predicted by the cascade model calculations [4, 12]. In the vicinity of ϵ_{max} the yield distribution depends strongly on the target (cf. fig. 2). In the case of the Cu target, we find that the data may only be explained if there is an accumulation of residues with excitation energies close to the limiting value. So at $\epsilon_1 < \epsilon \leq \epsilon_{max}$ we take

the parameterization

$$Y(\epsilon) \sim c_3 \cdot (-\alpha'(\epsilon)) \cdot exp(-c_2 \cdot (1 - \alpha(\epsilon))) \tag{5}$$

(in order to facilitate the random generation of the TNS ensemble we use here the function $\alpha(\epsilon)$, eq.(2), and its first derivative $\alpha'(\epsilon)$ with respect to ϵ). These two parameterizations are matched at $\epsilon = \epsilon_1 = 5$ MeV per nucleon. We chose the coefficients of the ensemble (2–5) by searching for the best description of the experimental data in the reaction ^{197}Au + Cu at 600 MeV per nucleon (see section 4). The resulting parameters are $c_1 = 0.16$, $c_2 = 0.26$, $c_3 = 6.7$, $\sigma_0 = 0.07$, and $c_0 = 2$.

It should be stressed that the suggested parameterization of the TNS ensemble cannot be unique and that the number of parameters is not essential. In principle, the ensemble could be presented in tabular form. It is important, however, that the whole ensemble is fully determined by the two independent experimental observables (i) the distribution of events as a function of their bound charge Z_{b3}, and (ii) the correlations between the multiplicities of intermediate-mass fragments and the bound charge. The simultaneous reproduction of other observables is a feature of the Statistical Multifragmentation Model.

In fig. 5 we show the distribution of TNS generated with expressions (2–5) in the mass versus energy plane. The projections on the mass and energy axes are given in the bottom part of the figure. The ensemble contains many nuclei with large masses and small excitation energies. There is also the accumulation of TNS with the highest excitations and diminishing masses which was necessary in order to reproduce the data. The explanation for this peculiarity of the residue population may be found in the physical picture of "overexcited" residues with $E_x/A > 8$ MeV which lose their energy and mass by preequilibrium emission until they reach thermodynamical equilibrium at $E_x/A < 8$ MeV. At lower bombarding energies or for more asymmetric collisions (like ^{197}Au + C in this experiment), when the energy transfer to the spectators is on average smaller, a comparable accumulation of highly excited residues is not expected (cf. fig. 2).

4 Comparison of model calculations and experimental data

In refs. [8-11] several observables were used to characterize the multi-fragment events: the summed bound charge Z_{bound} contained in all fragments with charges $Z \geq 2$; the multiplicity of intermediate-mass fragments M_{imf}; the maximum charge of fragments Z_{max}; the first asymmetry of fragments $A_{12} = (Z_{max} - Z_2)/(Z_{max} + Z_2)$ (here Z_2 is the charge of a second largest fragment); the second asymmetry $A_{23} = (Z_2 - Z_3)/(Z_2 + Z_3)$ (here Z_3 is the charge of a third largest fragment). The whole set of these observables gives a rather complete information about the fragmentation pattern. So M_{imf} is characterising the degree of disintegration of the TNS; Z_{max}, A_{12}, and A_{23} reflect the sizes of the fragments. From our analysis we have derived the conclusion that the statistical model, if it reproduces Z_{max}, A_{12}, and A_{23}, automatically gives good agreement for the yields of smaller-size fragments. The quantity Z_{bound} indicates directly the amount of nuclear matter contained in all fragments. The importance of such characteristics has been stressed already in ref. [17].

In this work we will exclude $Z = 2$ fragments from the bound charge and other observables for two reasons:

a) the detection of the very light reaction products is limited by the acceptance of the spectrometer (section 2).

b) α-particles, like nucleons, may originate from other processes not related to the fragmentation of the projectile spectator as, e.g., the primary interactions in the hot participant zone, the preequilibrium emission from hot fragments, or the coalescence of nucleons.

We will use the bound charge Z_{b3} which is the total charge contained in fragments with $Z \geq 3$. We will describe the measured absolute yields and distributions in M_{imf}, Z_{b3}, Z_{max}, A_{12} and A_{23}, all derived with a threshold set at $Z \geq 3$ (for the intermediate-mass fragments the definition $3 \leq Z \leq 30$ is used). For this purpose we have generated an ensemble of 10000 TNS as described in the previous section. The parameters for creating the ensemble were selected with the criterion to achieve a best description of the experimental distributions (section 3). The results are given in the following figures.

The experimental and theoretical distributions $d\sigma/dZ_{b3}$ for the ^{197}Au + Cu reaction are compared in fig. 6. The theoretical result was normalized with respect to the measured cross section in the region $Z_{b3} < 70$. The obtained normalization constant was then applied to all the calculated distributions which thus may be compared to the data on an absolute scale. At $Z_{b3} \geq 70$ the trigger effect is dominant, and neither the experimental nor the theoretical distribution should be considered realistic. No effort was made to improve the agreement in this region, and the difference will be visible in the corresponding parts of the charge correlations.

Figure 7 shows the mean values of the four observables M_{imf}, Z_{max}, A_{12}, and A_{23}, chosen to characterize the multifragmentation process, as a function of Z_{b3}. The agreement with the data is near perfect (except at the largest Z_{b3}). This is not very surprising since these data were the basis of the analysis leading to the chosen $\bar{A}/A_0$ versus E_x/A relation (eq.(2) and fig. 4). Apparently, the mean characteristics are entirely determined by this dependence and do not change with the relative yields of different TNS [12]. The experimental results are virtually identical for all targets although the yield distributions are qualitatively different, in particular in the lower part of the Z_{b3} range (fig. 2).

In contrast, the differential distributions for narrow bins of M_{imf} and Z_{b3} are very sensitive to the TNS ensemble and, therefore, contain information on the reaction dynamics. These distributions are given in figs. 8 to 13 for the reaction ^{197}Au on Cu. As mentioned before, all yields are given in absolute units (100 events correspond to 11.9 mb of cross section). Besides the overall normalization which relates the total number of model events to the measured cross section no additional adjustment was made. The agreement between the calculated and measured distributions is excellent. Substantial discrepancies are limited to the bin of large $Z_{b3} = 71$ to 80 where the effect of the experimental trigger prohibits a meaningful comparison.

In order to achieve a reasonable fit of the fragment asymmetry A_{12} we were forced to modify the expression for the bulk entropy of hot fragments. Instead of the usual expression $S^{bulk}_{A_f} = 2T \cdot A_f/\epsilon_0$, where $\epsilon_0 = 16$ MeV is the inverse level-density parameter used in our

previous work [3, 4], we introduce in ϵ_0 an additional A_f dependence of the form:

$$\epsilon_0(A_f) = \frac{\epsilon_0}{1 + c \cdot A_f^2}, \tag{6}$$

where c is a new adjustable parameter (which is actually very small $c \approx 3 \cdot 10^{-6}$). This modification may be justified by the fact that, due to the larger surface-to-volume ratio, smaller fragments cool down faster than heavier ones during their formation time. Therefore, one can expect that in the break-up configuration, when all fragments are already formed, smaller fragments may have lower excitation energy per nucleon than heavier ones. Without this modification the channels having two heavy fragments with approximately equal masses ("quasi-fission") will contribute very much to the total fragment production for large Z_{b3}. This would lead to a considerable rise of the calculated distributions for large Z_{b3} (fig. 12, right-hand side) in the region of small A_{12}. Although the correction is very small it suffices to suppress the "quasi-fission" in favour of a break-up of medium-hot residues ($E_x \approx 2$ to 3 MeV per nucleon) into two fragments of very different masses. It virtually does not change other characteristics nor the results at higher excitation energies.

Some of the distributions are affected by autocorrelation effects. In fig. 8 the definition $3 \leq Z \leq 30$ for intermediate-mass fragments requires $M_{imf} \geq 1$ for the three distributions with $1 \leq Z_{b3} \leq 30$. The condition $Z_{max} \leq Z_{b3}$ leads to discontinuities of the Z_{max} distributions at the boundaries of the Z_{b3} bins (fig. 11). The two bins with $Z_{b3} \geq 61$ are dominated by the trivial condition $Z_{max} = Z_{b3}$ valid for events where no other fragment with $Z \geq 3$ is produced. The asymmetries A_{12} and A_{23} (figs. 12, 13) are rational numbers by definition. For small Z_{b3} the number of possible values that they may assume is small and more widely separated than the chosen bin size. This effect dominates the shapes of the distributions in these bins. Finally, the asymmetries reflect features of the multiplicity distributions in the sense that only events with at least two and three fragments with $Z \geq 3$ contribute to the A_{12} and A_{23} distributions, respectively.

Several of the experimental distributions exhibit characteristics that are related to the rise and fall of the multi-fragment production as Z_{b3} decreases from the largest to the smallest values (fig. 7, top). Both, the Z_{b3} (fig. 9) and the Z_{max} (fig. 10) distributions are doubly humped at small M_{imf}, where mainly events from the rise and the fall regions

are sampled, and evolve into more bell shaped distributions as M_{imf} increases. The M_{imf} distributions (fig. 8) follow the rise and fall but, at the same time, exhibit a characteristic difference between the processes that are dominant in the rise and in the fall regime. The distributions have asymmetric shapes with long tails towards large M_{imf} for large Z_{b3} (fig. 8, right-hand side) and evolve to nearly symmetric shapes with decreasing mean value and width as Z_{b3} decreases (fig. 8, left-hand side). In the rise regime (large Z_{b3}) the most probable value of M_{imf} is smaller than the mean. At the same time the probability that a heavy nucleus survives is large as reflected by the Z_{max} (fig. 11) and the A_{12} (fig. 12) distributions; the latter show a strong weighting towards large asymmetries for large Z_{b3}. In contrast, they are nearly flat over the full range of possible asymmetries for $20 \leq Z_{b3} \leq 40$ where the fragment multiplicities assume their maximum value.

We can try to summarize the disintegration scenario for the ^{197}Au on Cu reaction as it appears on the basis of this analysis. In the most peripheral collisions a large residual nucleus with low excitation is produced which, later on, undergoes fission and deexcitation by evaporation cascades. In semi-central collisions more energy is transferred to the spectators and more particles are emitted at the preequilibrium stage. As a result, smaller residues with higher excitation are formed and their breaking-up into two, three and more fragments becomes the dominant channel. In the transition region, corresponding to $Z_{b3} = 50 - 70$ where M_{imf} is on the rise, the large asymmetry A_{12} (the largest fragment is considerably larger than the others), the asymmetric multiplicity distribution, and the very small number of events with two approximately equally large fragments mean that here the formation of heavy-residues is still likely and that fission is suppressed at these high excitations. Fission takes place mainly in compound nuclei of low excitation. Another important conclusion is the following: The decrease of the fragment multiplicities towards more central collisions (at $Z_{b3} < 30$) is not due to increasing excitations but rather decreasing masses of the TNS.

5 Conclusion

We have presented new data on the fragmentation of ^{197}Au projectiles of $E/A = 600$ MeV in collisions with C, Al, Cu, and Pb targets, thus complementing previous reports on these experiments [8-11]. In particular, we have reported absolute cross sections, mean helium multiplicities, N/Z ratios for the detected fragments, and differential distributions of the charge observables M_{imf}, Z_{b3}, Z_{max}, A_{12}, and A_{23}.

The theoretical analysis of the ^{197}Au + Cu reaction is based on the Statistical Multifragmentation Model as developed in refs. [3, 4, 17]. The main results and conclusions derived from the comparison to the experimental data are the following:

1) With the model assumption, that intermediate-mass fragments are produced in the break-up of equilibrated sources, a good description of the data is achieved. It is absolute apart from an overall normalization constant that relates the number of model events to the measured cross section.

2) Using the model we were able to reconstruct a "realistic" ensemble of thermalized nuclear systems (TNS) formed after the nonequilibrium stage of the reaction. The parameters of the TNS distribution are fully determined by the criterion of a best fit to the full ensemble of observables.

3) On that basis the data are consistent with a saturation of the TNS excitation energies at values of $E_x/A \approx 8$ MeV which is ascribed to prequilibrium emission prior to TNS formation. The ensemble reconstructed for the reaction ^{197}Au + C exhibits an accumulation of TNS with excitation energies close to this limit.

A.S. Botvina would like to thank the GSI for the kind hospitality and for financial support. I.N.Mishustin is grateful to the Institute of Theoretical Physics of Frankfurt University for the kind hospitality and the Deutsche Forschungsgemeinschaft for financial support.

References

[1] B. Jakobsson, G. Jönsson, B. Lindkvist, and A. Oskarsson, Z. Phys. A307 (1982) 293.

[2] for a review see, e.g., L.G. Moretto and G.J. Wozniak, Ann Rev. Nucl. Part. Science 43 (1993) 379.

[3] A.S. Botvina, A.S. Iljinov, I.N. Mishustin, J.P. Bondorf, R. Donangelo, and K. Sneppen, Nucl. Phys. A475 (1987) 663.

[4] A.S. Botvina, A.S. Iljinov, and I.N. Mishustin, Nucl. Phys. A507 (1990) 649.

[5] D.H.E. Gross, Rep. Prog. Phys. 53 (1990) 605.

[6] D.R. Bowman, G.F. Peaslee, R.T. de Souza, N. Carlin, C.K. Gelbke, W.G. Gong, Y.D. Kim, M.A. Lisa, W.G. Lynch, L. Phair, M.B. Tsang, C. Williams, N. Colonna, K. Hanold, M.A. McMahan, G.J. Wozniak, L.G. Moretto, and W.A. Friedman, Phys. Rev. Lett. 67 (1991) 1527.

[7] R.T. de Souza, L. Phair, D.R. Bowman, N. Carlin, C K. Gelbke, W.G. Gong, Y.D. Kim, M.A. Lisa, W.G. Lynch, G.F. Peaslee, M.B. Tsang, H.M. Xu, F. Zhu, and W.A. Friedman, Phys. Lett. B268 (1991) 6.

[8] J. Hubele, P. Kreutz, V. Lindenstruth, J.C. Adloff, M. Begemann-Blaich, P. Bouissou, G. Imme, I. Iori, G.J. Kunde, S. Leray, Z. Liu, U. Lynen, R.J. Meijer, U. Milkau, A. Moroni, W.F.J. Müller, C. Ngô, C.A. Ogilvie, J. Pochodzalla, G. Raciti, G. Rudolf, H. Sann, A. Schüttauf, W. Seidel, L. Stuttge, W. Trautmann, A. Tucholski, R. Heck, A.R. DeAngelis, D.H.E. Gross, H.R. Jaqaman, H.W. Barz, H. Schulz, W.A. Friedman, and R.J. Charity, Phys. Rev. C46 (1992) R1577.

[9] P. Kreutz, J.C. Adloff, M. Begemann-Blaich, P. Bouissou, J. Hubele, G. Imme, I. Iori, G.J. Kunde, S. Leray, V. Lindenstruth, Z. Liu, U. Lynen, R.J. Meijer, U. Milkau, A. Moroni, W.F.J. Müller, C. Ngô, C.A. Ogilvie, J. Pochodzalla, G. Raciti, G. Rudolf, H. Sann, A. Schüttauf, W. Seidel, L. Stuttge, W. Trautmann, and A. Tucholski, Nucl. Phys. A556 (1993) 672.

[10] C.A. Ogilvie, J.C. Adloff, M. Begemann-Blaich, P. Bouissou, J. Hubele, G. Imme, I. Iori, P. Kreutz G.J. Kunde, S. Leray, V. Lindenstruth, Z. Liu, U. Lynen, R.J. Meijer, U. Milkau, W.F.J. Müller, C. Ngô, J. Pochodzalla, G. Raciti, G. Rudolf, H. Sann, A. Schüttauf, W. Seidel, L. Stuttge, W. Trautmann, and A. Tucholski, Phys. Rev. Lett. 67 (1991) 1214.

[11] J. Hubele, P. Kreutz, J.C. Adloff, M. Begemann-Blaich, P. Bouissou, G. Imme, I. Iori, G.J. Kunde, S. Leray, V. Lindenstruth, Z. Liu, U. Lynen, R.J. Meijer, U. Milkau, A. Moroni, W.F.J. Müller, C. Ngô, C.A. Ogilvie, J. Pochodzalla, G. Raciti, G. Rudolf, H. Sann, A. Schüttauf, W. Seidel, L. Stuttge, W. Trautmann, and A. Tucholski, Z. Phys. A 340 (1991) 263.

[12] A.S. Botvina and I.N. Mishustin, Phys. Lett. B294 (1992) 23.

[13] H.W. Barz, W. Bauer, J.P. Bondorf, A.S. Botvina, R. Donangelo, H. Schulz, and K. Sneppen, Nucl. Phys. A561 (1993) 466.

[14] Bao-An Li, A.R. DeAngelis, and D.H.E. Gross, Phys. Lett B303 (1993) 225.

[15] V. Lindenstruth, PhD thesis, Universität Frankfurt, 1993, report GSI-93-18.

[16] K. Sümmerer, W. Brüchle, D.J. Morrissey, M. Schädel, B Szweryn, and Y. Weifan, Phys. Rev. C42, 2546 (1990).

[17] A.S. Botvina, A.S. Iljinov, and I.N. Mishustin, Sov. J. Nucl. Phys. 42 (5) (1985) 712.

[18] G.D. Adeev, A.S. Botvina, A.S. Iljinov, M.V. Mebel, N.I. Pischasov, and O.N. Serdyuk, Preprint INR, P-816/93, Moscow, 1993.

Figure Captions

Fig. 1. Mean multiplicity of $Z = 2$ particles detected with the time-of-flight wall as a function of the bound charge Z_{bound} for the reactions of ^{197}Au projectiles with C (full line), Al (dashed), Cu (dashed-dotted), and Pb (dotted) targets at $E/A = 600$ MeV.

Fig. 2. Measured cross sections $d\sigma/dZ_{bound}$ (top) and $d\sigma/dZ_{b3}$ (bottom) for the reactions of ^{197}Au projectiles with C (full line), Al (dashed), Cu (dashed-dotted), and Pb (dotted) targets at $E/A = 600$ MeV. Note that, with the vertical scale chosen for optimum representation, the lowest channels for the Pb target are out of range; the measured values are 340 mb ($Z_{bound} = 0$), 240 mb ($Z_{bound} = 2$), 850 mb ($Z_{b3} = 0$), and 310 mb ($Z_{b3} = 3$).

Fig. 3. Measured N/Z (top) and mean value $\langle N/Z \rangle$ (bottom) as a function of the atomic number Z of projectile fragments from the reaction ^{197}Au + Cu at $E/A = 600$ MeV. The lines in the top panel represent the valley of stability according to the Weizsaecker mass formula (long dashed) and the EPAX parameterization [16] (short dashed). In the bottom panel, the experimental data are given by the open circles and the prediction of the Statistical Multifragmentation Model by the histogram.

Fig. 4. Correlation of relative mass A/A_0 ($A_0 = 197$) and excitation energy E_x/A of thermalized nuclear systems produced after the nonequilibrium stage in the ^{197}Au + C, Al, Cu, and Pb reactions at $E/A = 600$ MeV. The results of the analyses of the Moscow [12], Berlin [14], and Copenhagen [13] groups are given by circles, triangles, and squares, respectively. The solid curve and the vertical bars represent the mean correlation (eq.(2)) and the widths (eq. (3)) of the ensemble as suggested in this work.

Fig. 5. Top: Correlation of relative mass A/A_0 ($A_0 = 197$) and excitation energy E_x/A of thermalized nuclear systems for the reaction ^{197}Au + Cu at $E/A = 600$ MeV as obtained from the present analysis. The binnings are 0.05 for A/A_0 and 0.5 MeV for E_x/A, the areas of the squares are proportional to the number of nuclei in these bins.
Bottom: The projected distributions of mass A/A_0 and energy E_x/A.

Fig. 6. Absolute cross section of fragmentation events as a function of the bound charge Z_{b3} for the ^{197}Au + Cu reaction at $E/A = 600$ MeV. The data were used to determine the yield parameters and the overall normalization of the calculated yields (histogram) relative to the experiment (open circles).

Fig. 7. Mean values of the multiplicity of intermediate-mass fragments $\langle M_{imf} \rangle$, the maximum fragment charge $\langle Z_{max} \rangle$, and of the first and second fragment asymmetries $\langle A_{12} \rangle$ and $\langle A_{23} \rangle$ versus the bound charge Z_{b3} for the reactions ^{197}Au on C (triangles), Al (squares), and Cu (circles) at $E/A = 600$ MeV. A threshold of $Z \geq 3$ was required for all observables. The results calculated for ^{197}Au on Cu are given by the histogram.

Fig. 8. Distributions of the multiplicity M_{imf} of intermediate-mass fragments for the indicated bins of Z_{b3} for the reaction ^{197}Au on Cu at $E/A = 600$ MeV. The measured data and the calculated results are represented by the open circles and by the histogram, respectively.

Fig. 9. Distributions of the bound charge Z_{b3} of fragmentation events for the indicated values of M_{imf} for the reaction ^{197}Au on Cu at $E/A = 600$ MeV. The measured data and the calculated results are represented by the open circles and by the histogram, respectively.

Fig. 10. Distributions of of the atomic number Z_{max} of the largest fragment within an event for the indicated values of M_{imf} for the reaction ^{197}Au on Cu at $E/A = 600$ MeV. The measured data and the calculated results are represented by the open circles and by the histogram, respectively.

Fig. 11. Distributions of of the atomic number Z_{max} of the largest fragment within an event for the indicated bins of Z_{b3} for the reaction ^{197}Au on Cu at $E/A = 600$ MeV. The measured data and the calculated results are represented by the open circles and by the histogram, respectively.

Fig. 12. Distributions of the charge asymmetry A_{12} of the two largest fragments for the indicated bins of Z_{b3} for the reaction ^{197}Au on Cu at $E/A = 600$ MeV. Events with at

least two fragments with $Z \geq 3$ have been selected. The measured data and the calculated results are represented by the open circles and by the histogram, respectively.

Fig. 13. Distributions of the charge asymmetry A_{23} of the second and third largest fragments for the indicated bins of Z_{b3} for the reaction ^{197}Au on Cu at $E/A = 600$ MeV. Events with at least three fragments with $Z \geq 3$ have been selected. The measured data and the calculated results are represented by the open circles and by the histogram, respectively.

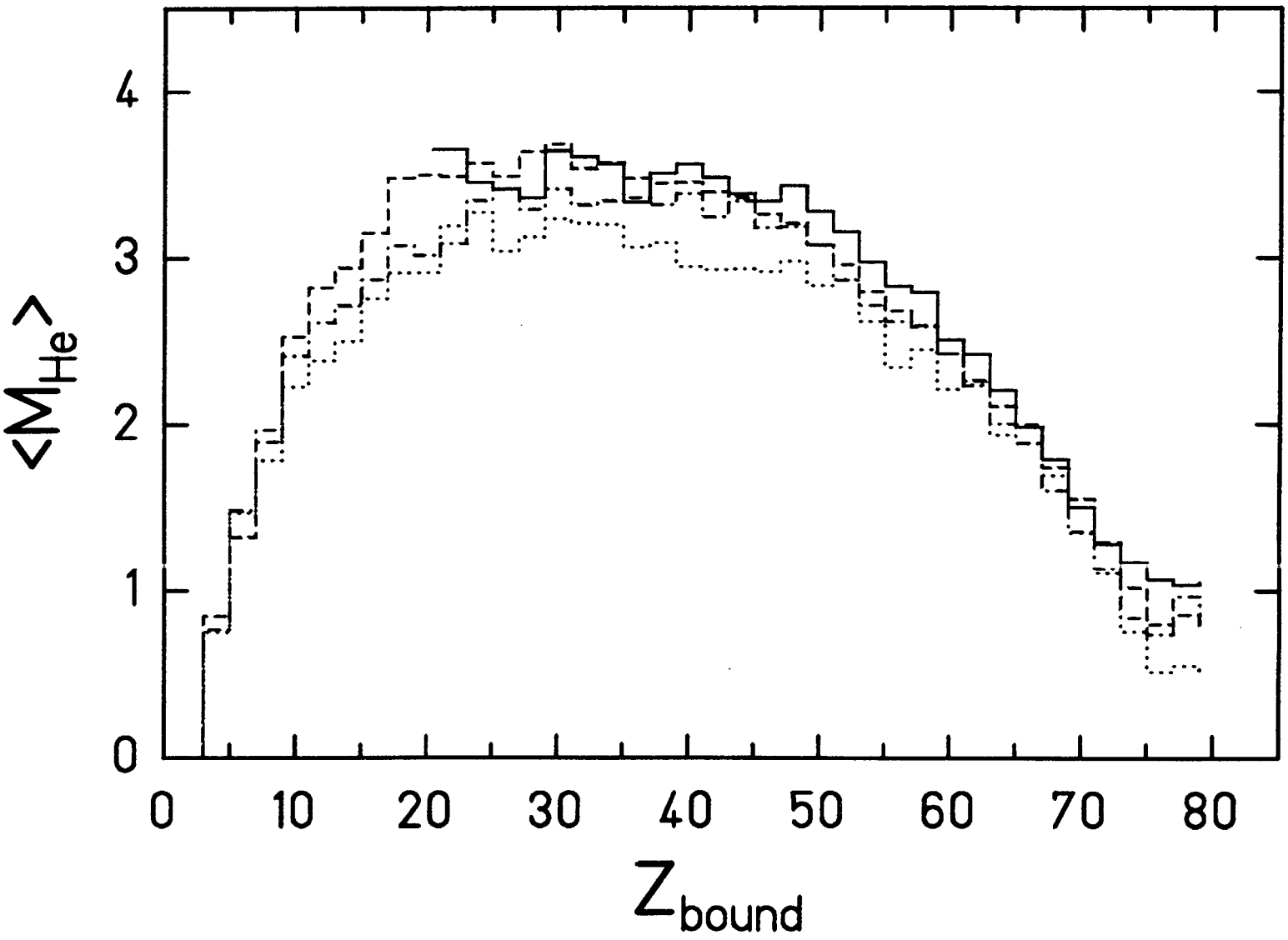

Fig. 1

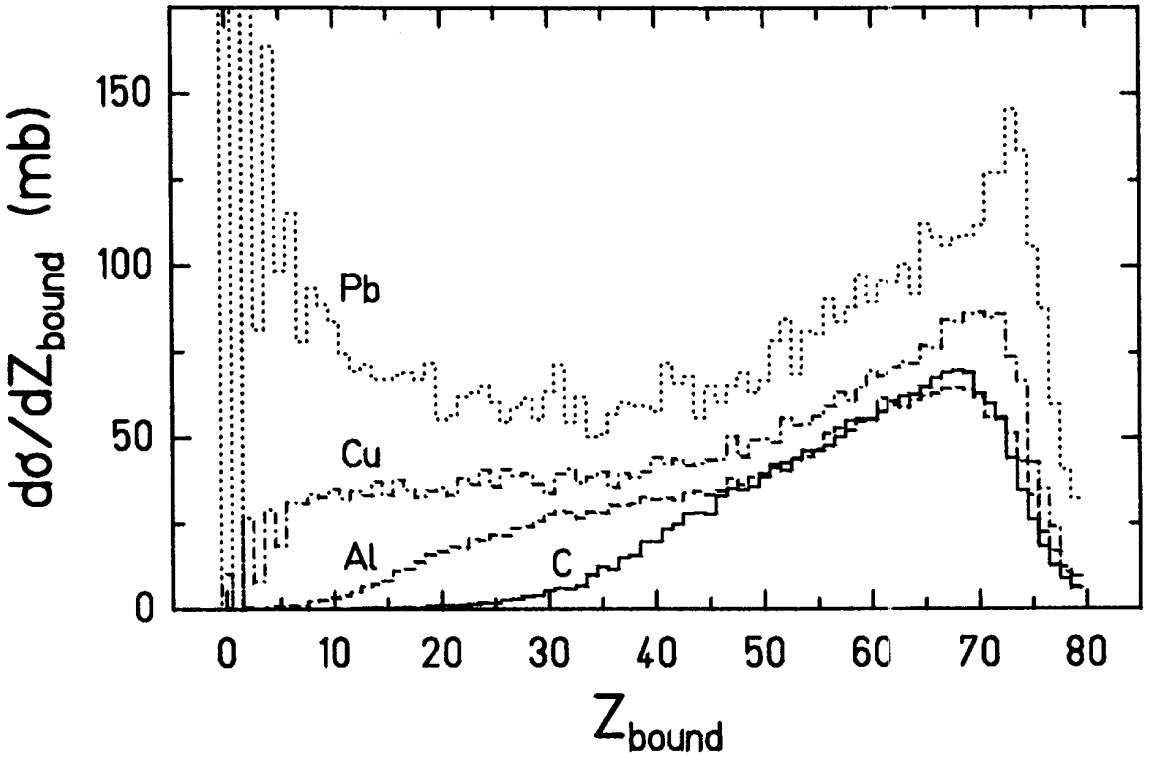
dσ/dZ_bound (mb)
150
100
50
0
Pb
Cu
Al
C
0
10
20
30
40
50
60
70
80
Z_bound

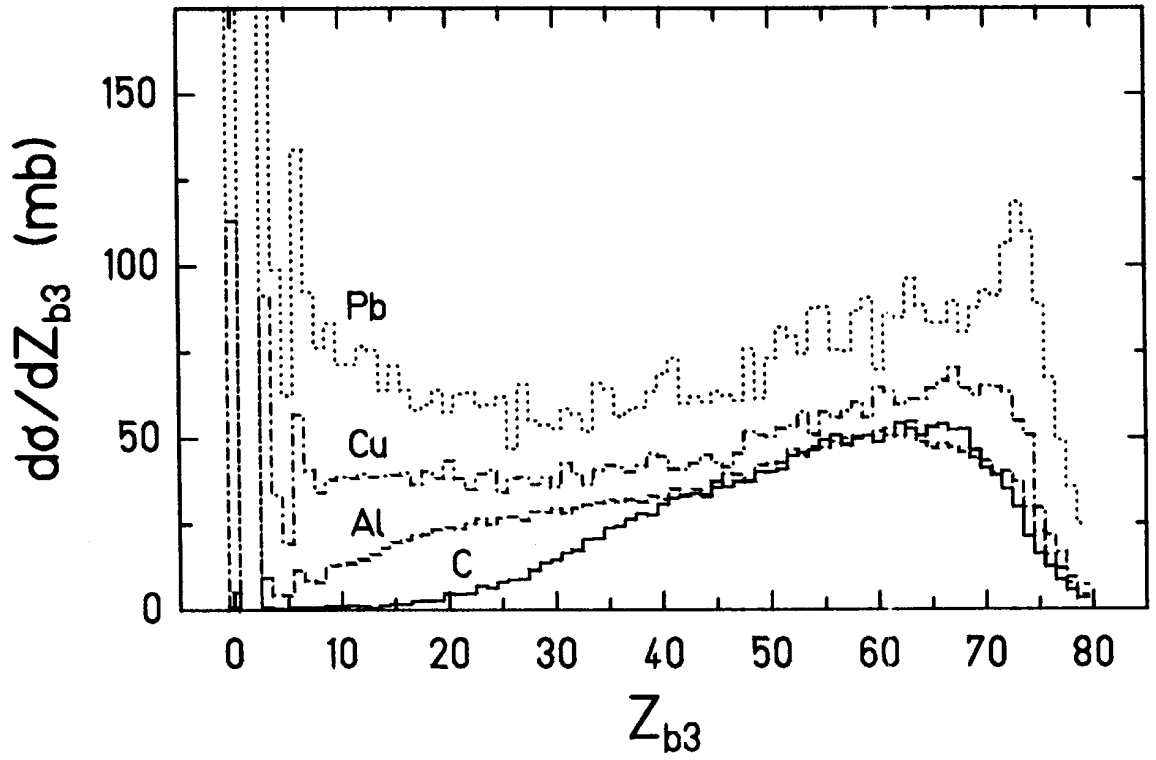
dσ/dZ_b3 (mb)
150
100
50
0
Pb
Cu
Al
C
0
10
20
30
40
50
60
70
80
Z_b3

Fig. 2

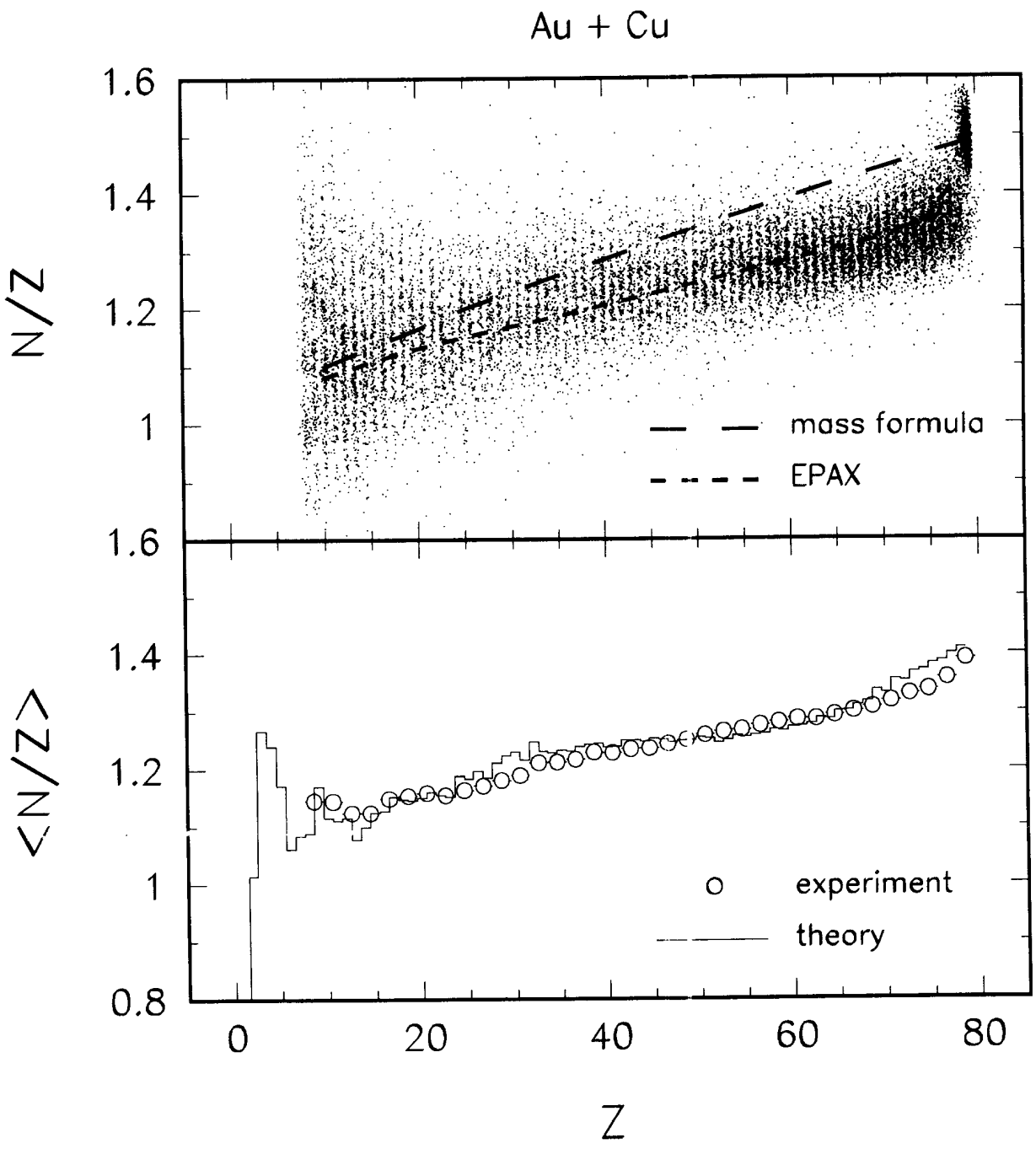
Au + Cu
N/Z
1.6
1.4
1.2
1
mass formula
EPAX
<N/Z>
1.6
1.4
1.2
1
0.8
experiment
theory
0
20
40
60
80
Z

Fig. 3

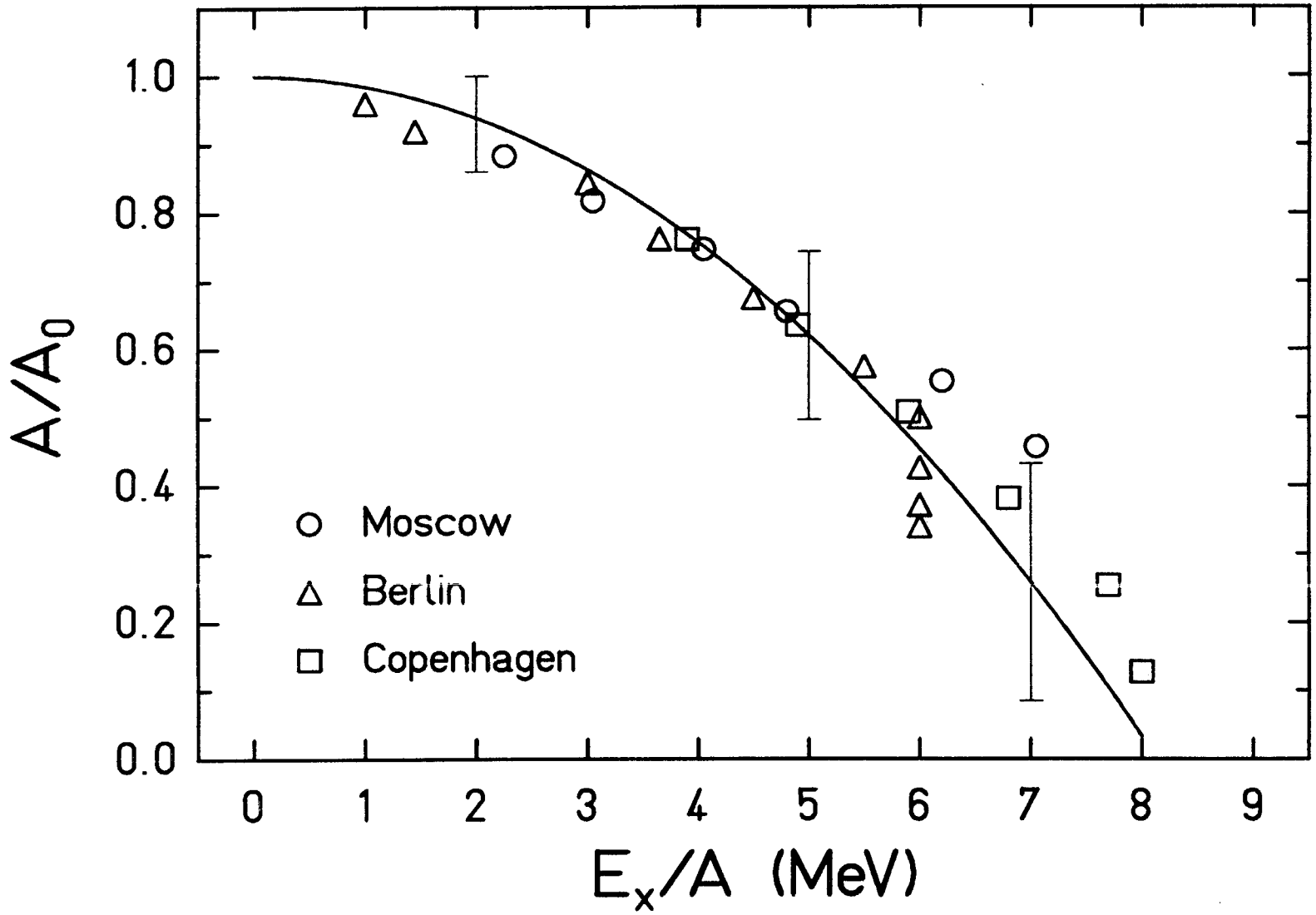
1.0
0.8
0.6
0.4
0.2
0.0
A/A0
Moscow
Berlin
Copenhagen
0
1
2
3
4
5
6
7
8
9
Ex/A (MeV)

Fig. 4

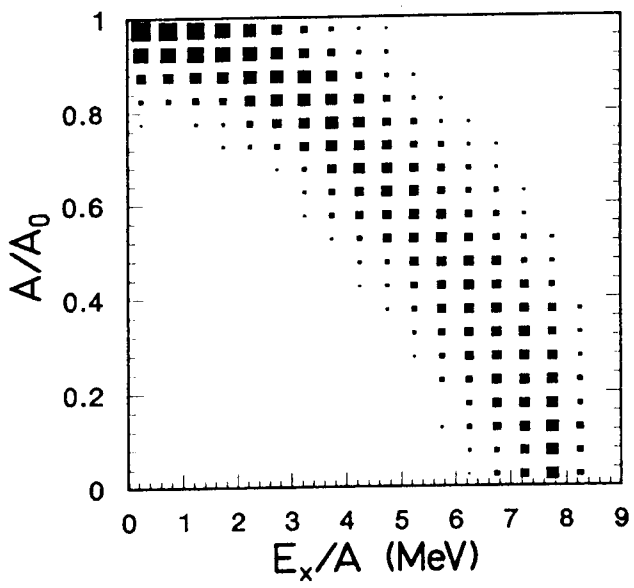

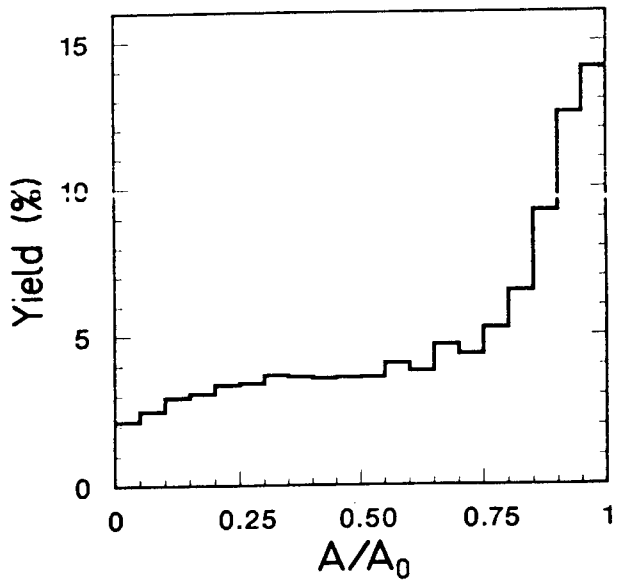

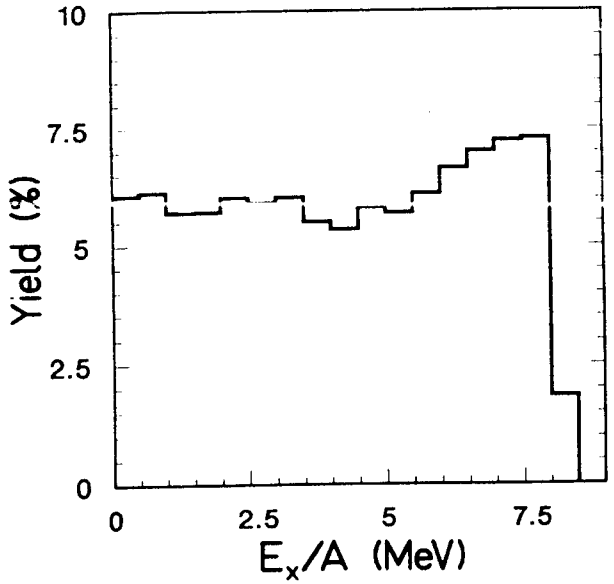

Fig. 5

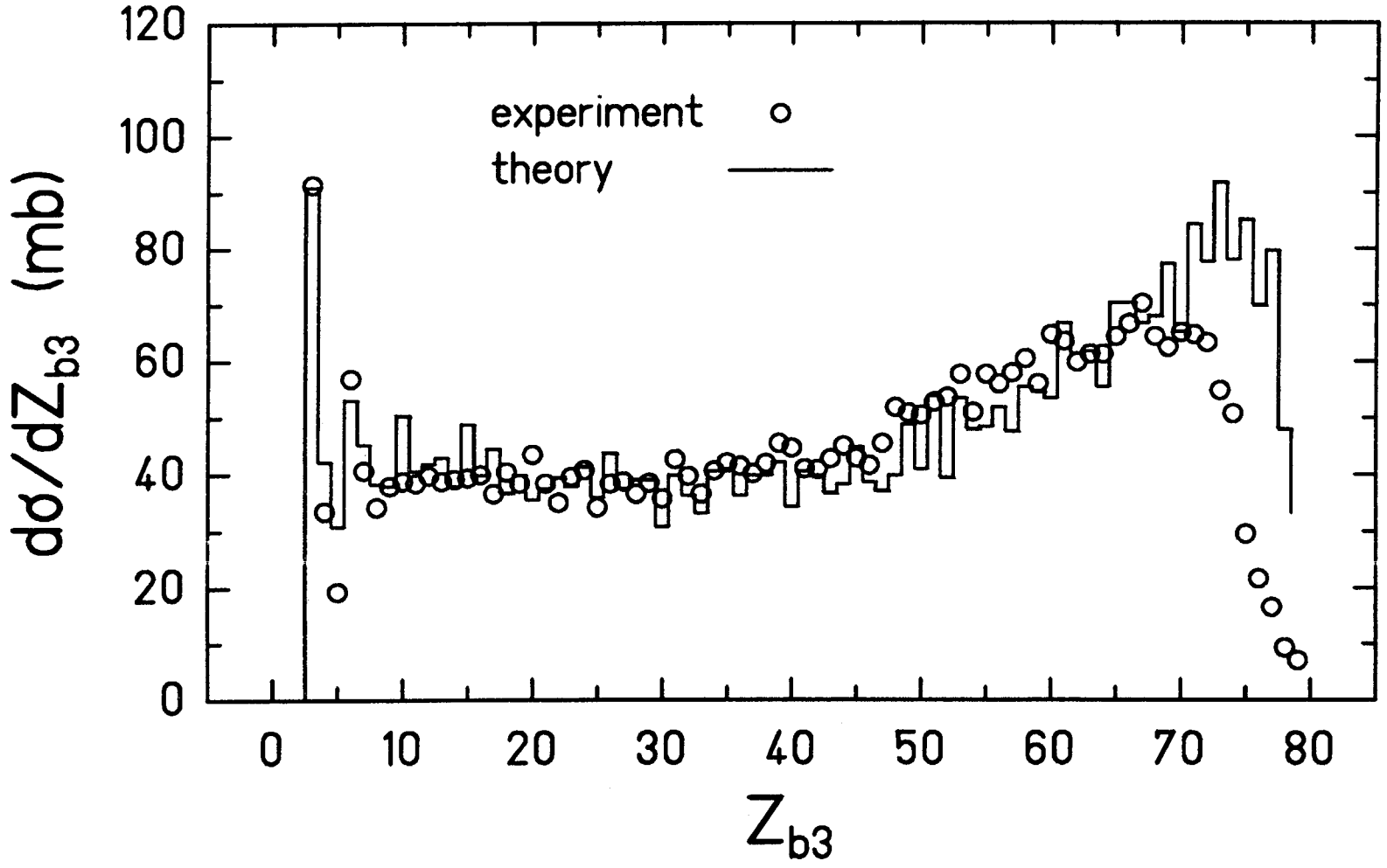
experiment
theory
dσ/dZ_b3 (mb)
Z_b3
0
20
40
60
80
100
120
0
10
20
30
40
50
60
70
80

Fig. 6

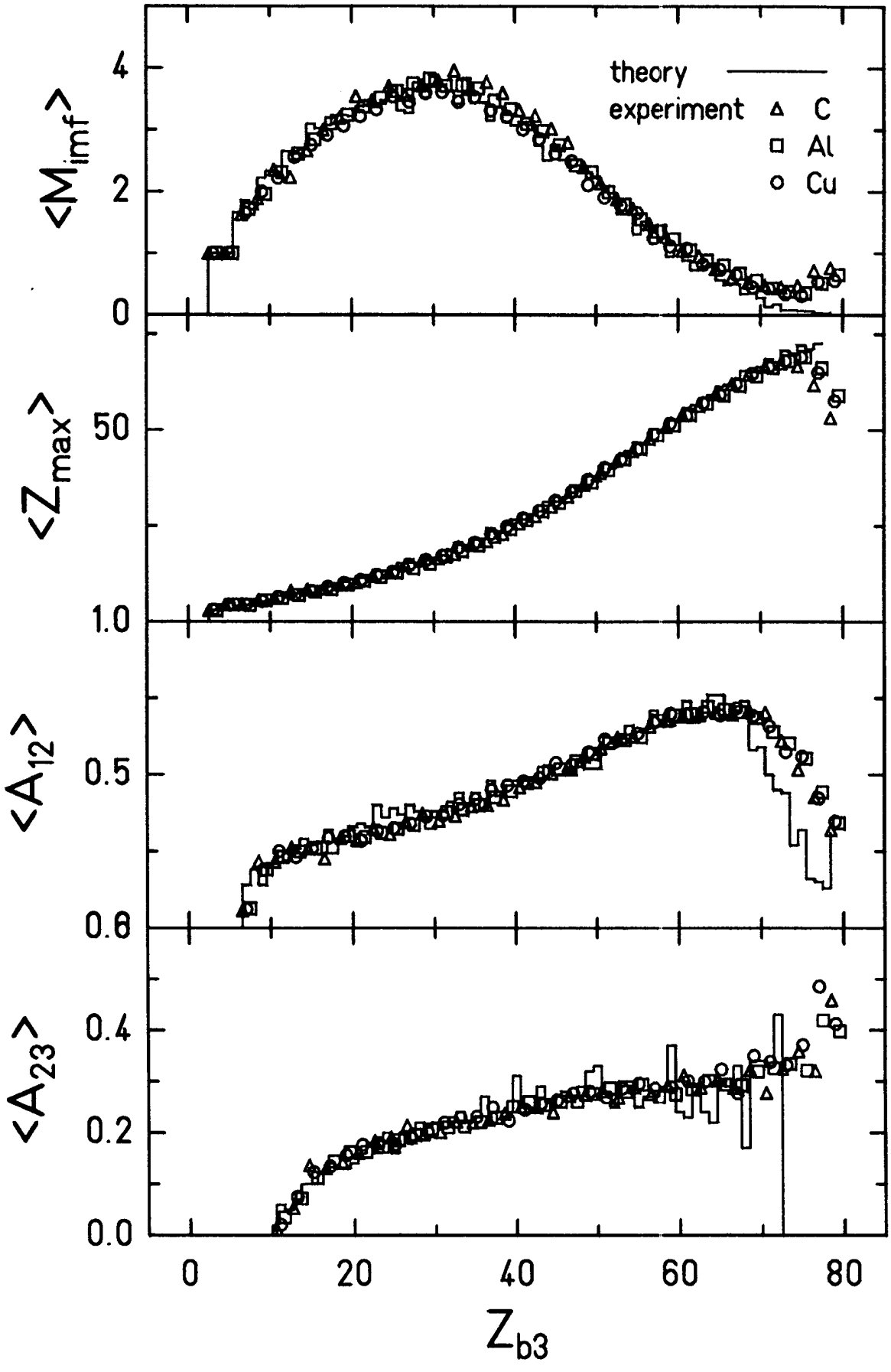
theory
experiment
C
Al
Cu
<M_imf>
<Z_max>
<A_12>
<A_23>
Z_b3
0
20
40
60
80
0.0
0.2
0.4
0.6
0.5
1.0
50
2
4

Fig. 7

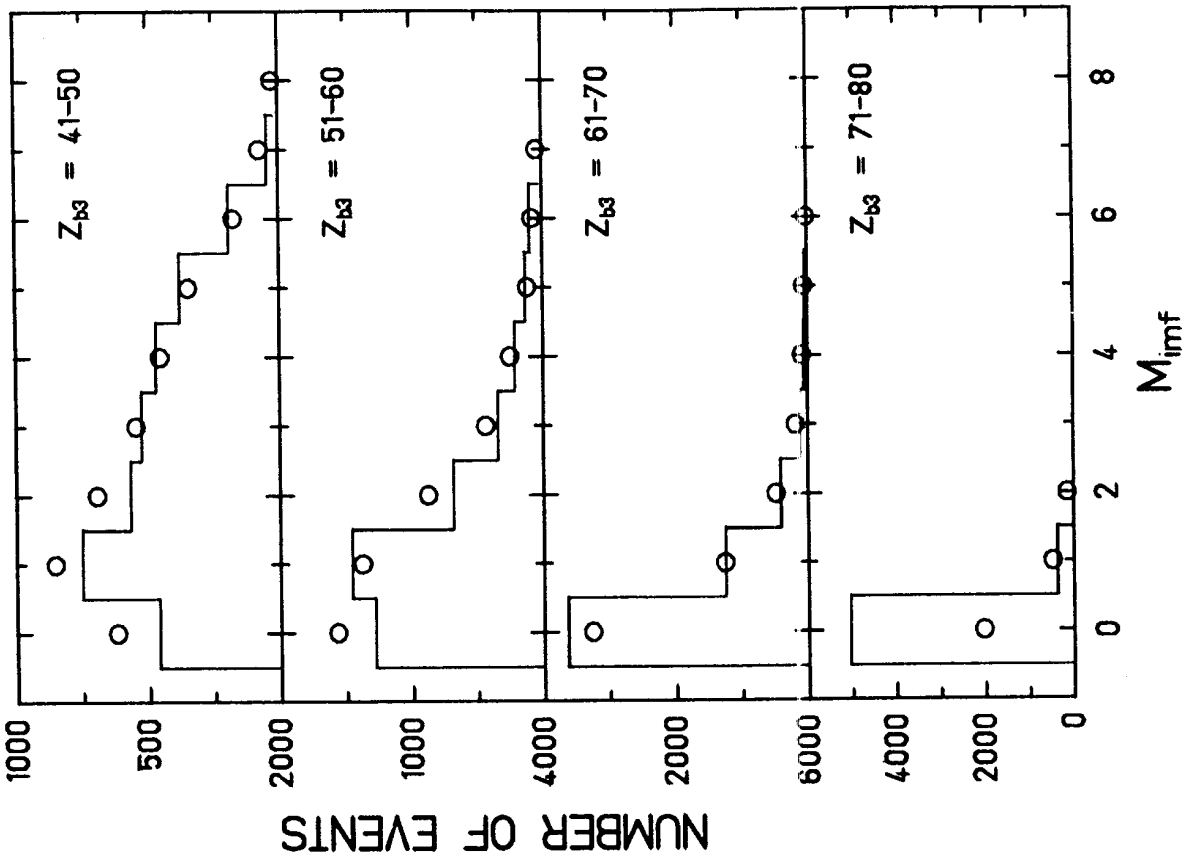
NUMBER OF EVENTS
Z_{b3} = 41-50
Z_{b3} = 51-60
Z_{b3} = 61-70
Z_{b3} = 71-80
M_{imf}

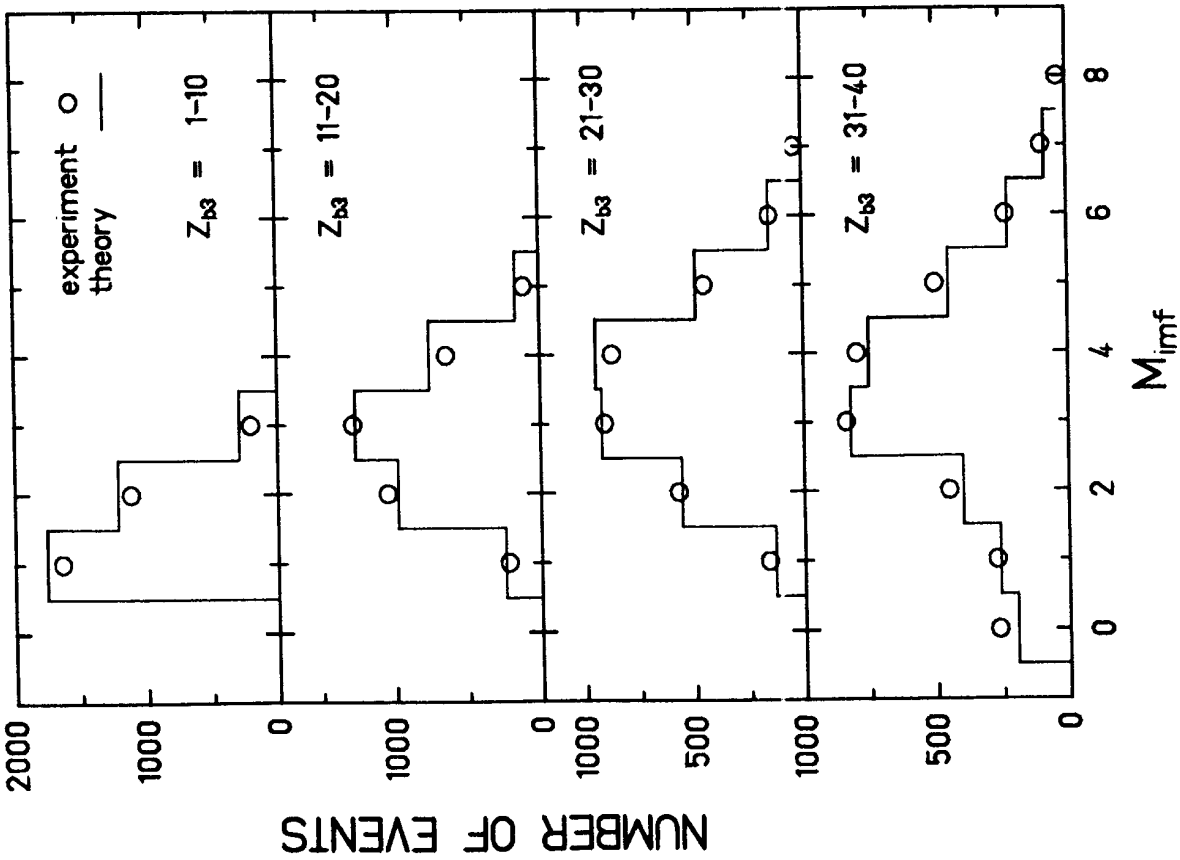
NUMBER OF EVENTS
experiment o
theory —
Z_{b3} = 1-10
Z_{b3} = 11-20
Z_{b3} = 21-30
Z_{b3} = 31-40
M_{imf}

Fig. 8

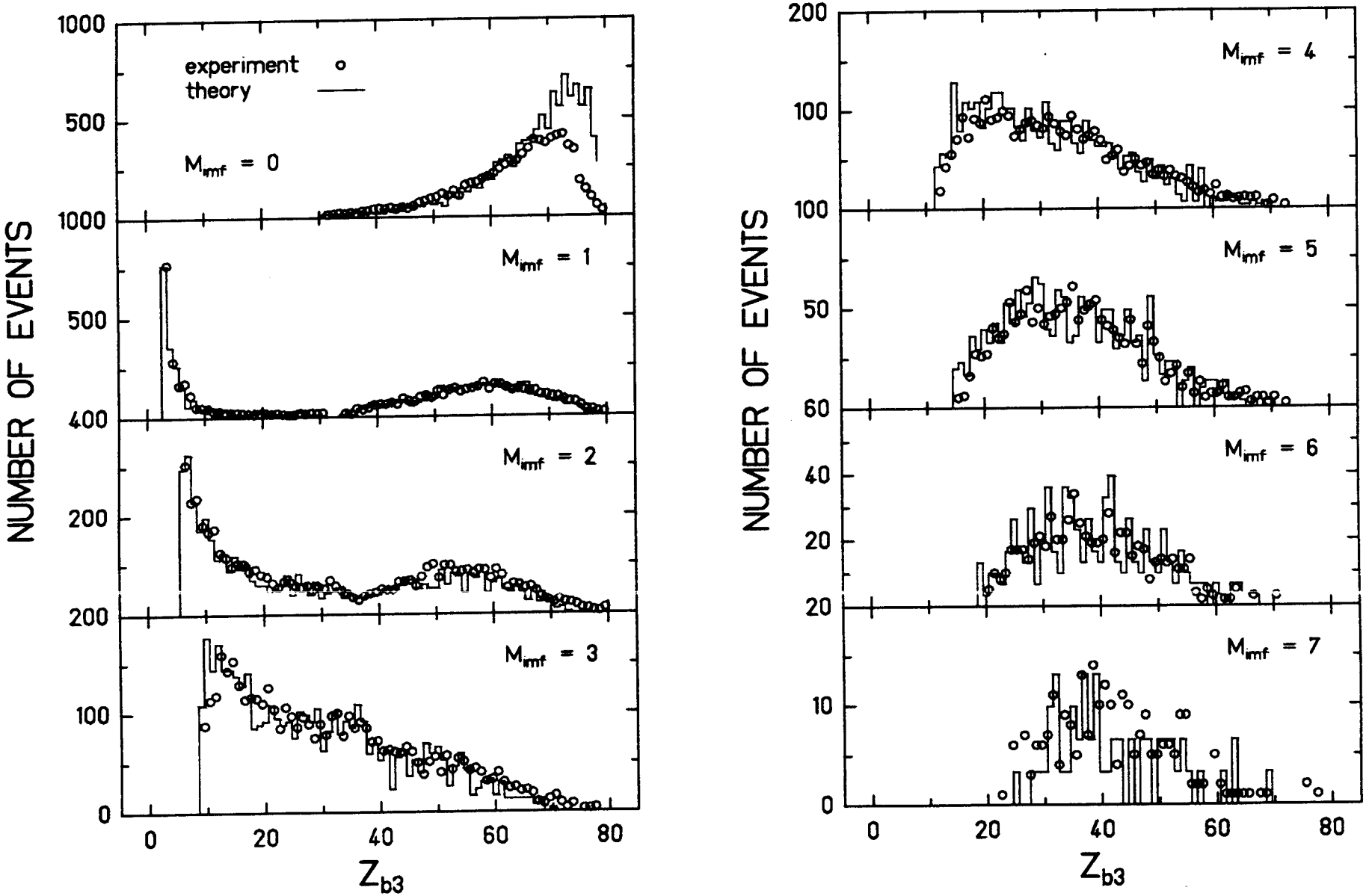
NUMBER OF EVENTS
experiment
theory
M_{imf} = 0
M_{imf} = 1
M_{imf} = 2
M_{imf} = 3
M_{imf} = 4
M_{imf} = 5
M_{imf} = 6
M_{imf} = 7
Z_{b3}
Z_{b3}

Fig. 9

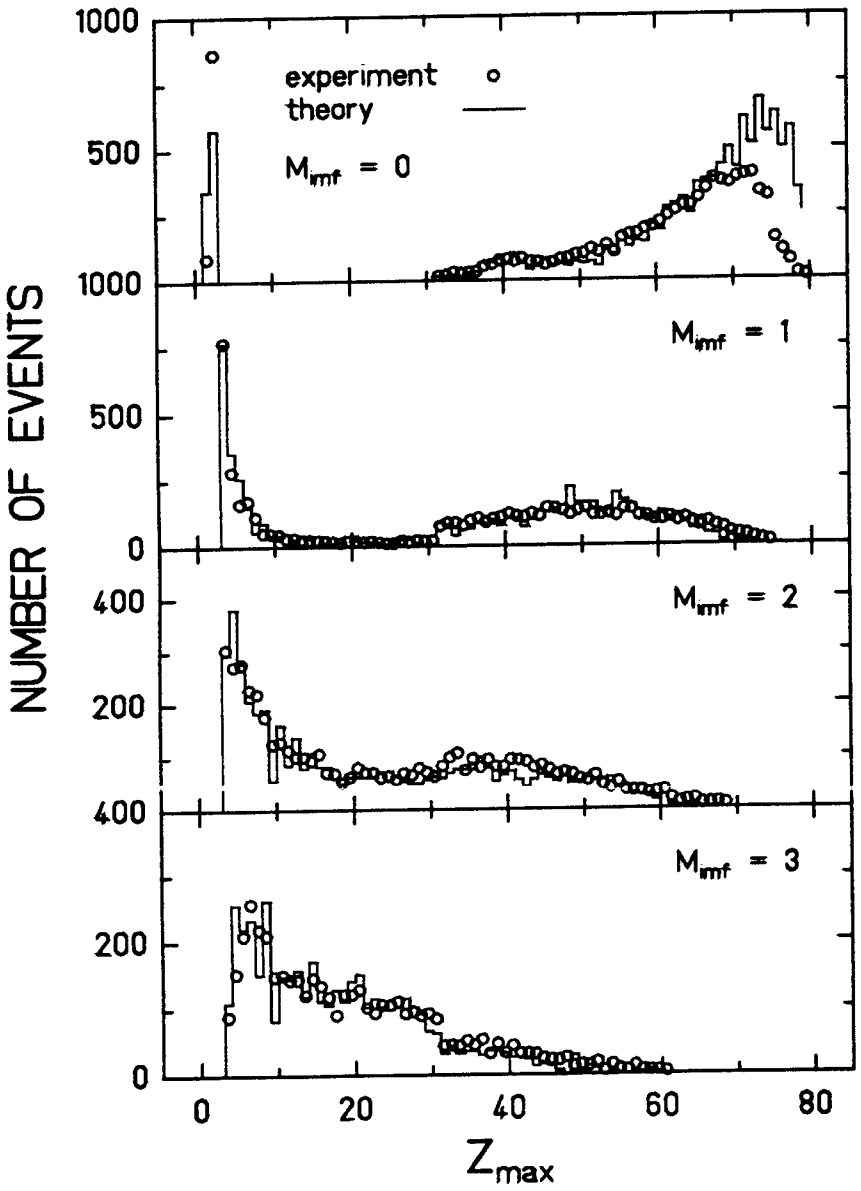
NUMBER OF EVENTS
experiment
theory
M_{imf} = 0
M_{imf} = 1
M_{imf} = 2
M_{imf} = 3
Z_{max}

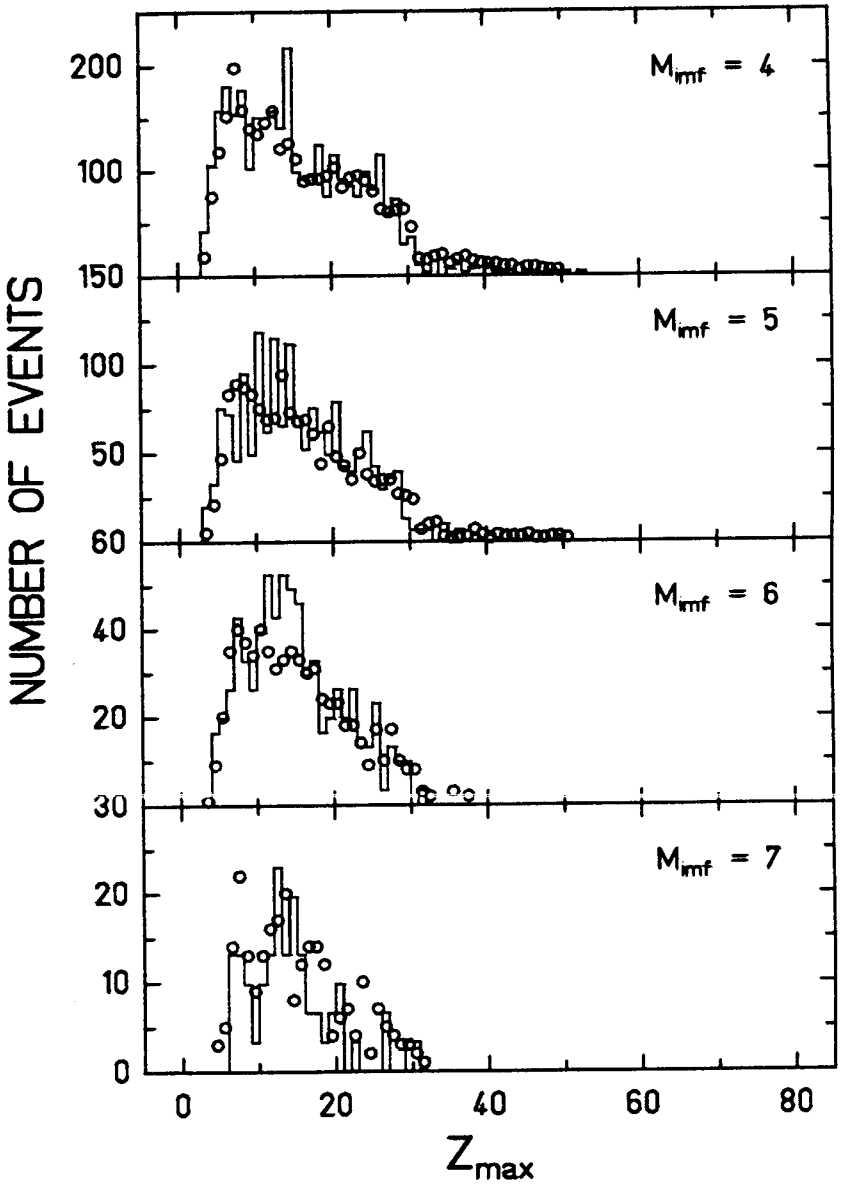
NUMBER OF EVENTS
M_{imf} = 4
M_{imf} = 5
M_{imf} = 6
M_{imf} = 7
Z_{max}

Fig. 10

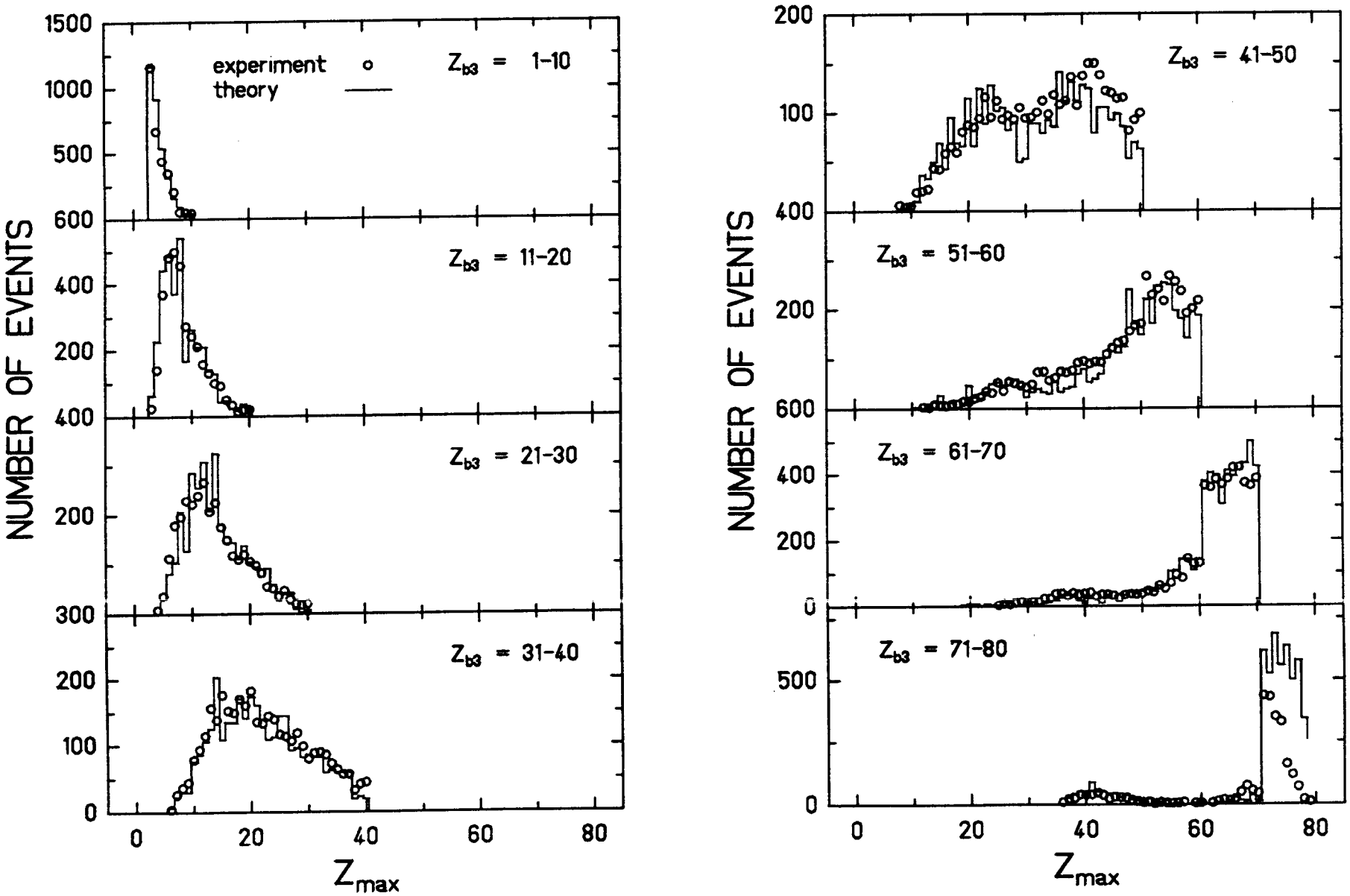
NUMBER OF EVENTS
experiment
theory
Z_{b3} = 1-10
Z_{b3} = 11-20
Z_{b3} = 21-30
Z_{b3} = 31-40
Z_{b3} = 41-50
Z_{b3} = 51-60
Z_{b3} = 61-70
Z_{b3} = 71-80
Z_{max}

Fig. 11

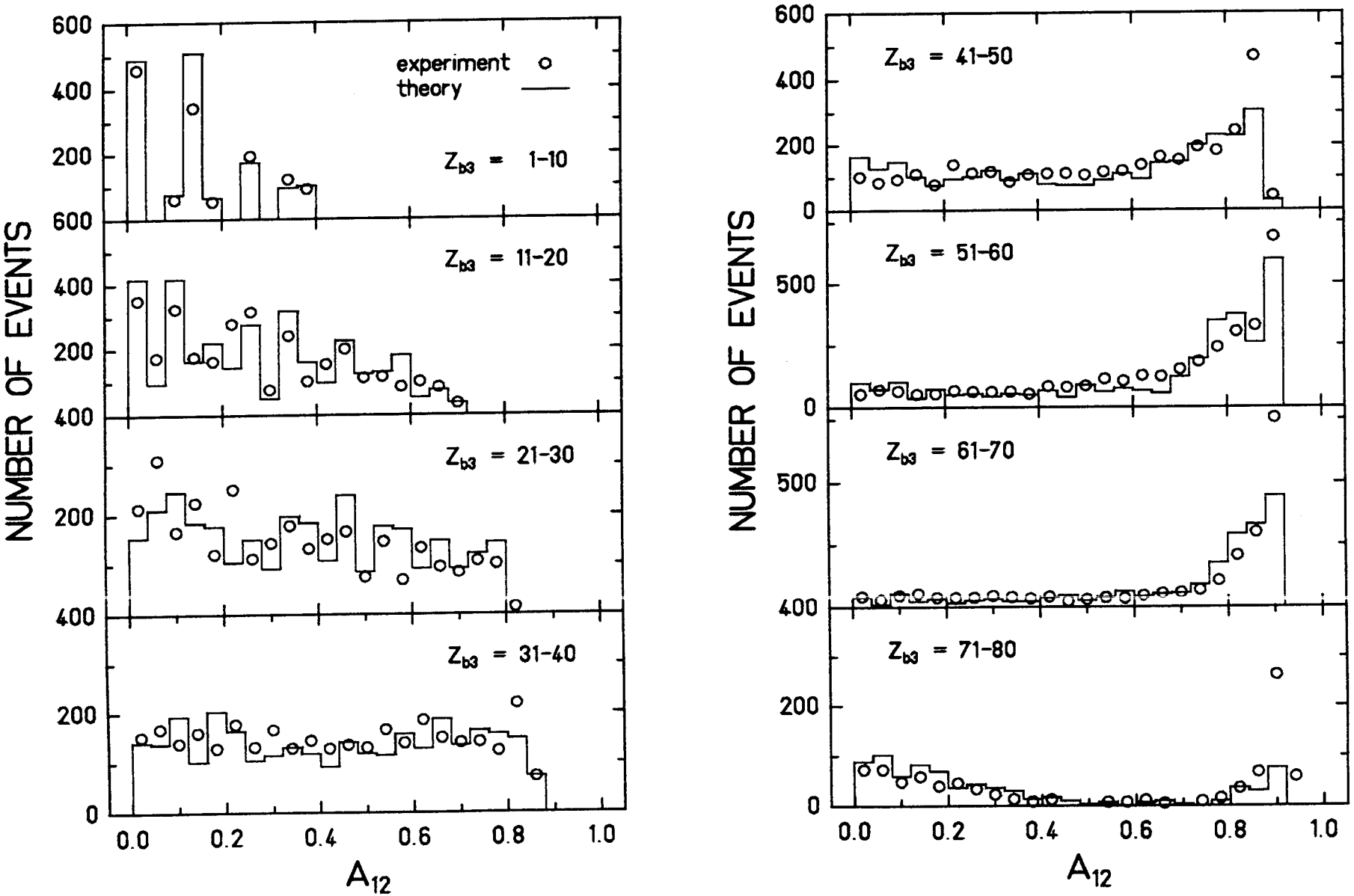
NUMBER OF EVENTS
experiment
theory
Z_{b3} = 1-10
Z_{b3} = 11-20
Z_{b3} = 21-30
Z_{b3} = 31-40
Z_{b3} = 41-50
Z_{b3} = 51-60
Z_{b3} = 61-70
Z_{b3} = 71-80
A_{12}
0.0
0.2
0.4
0.6
0.8
1.0

Fig. 12

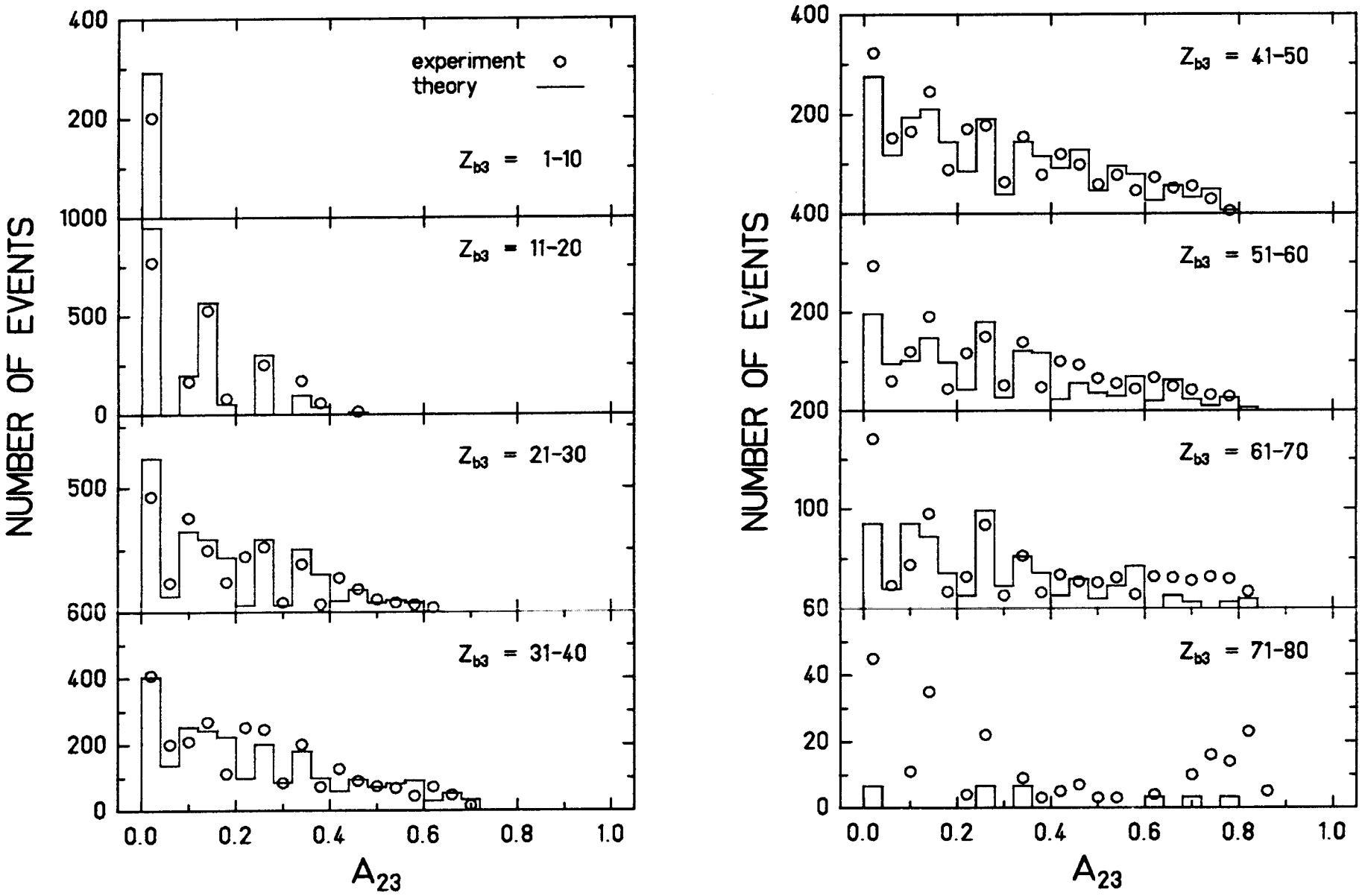
NUMBER OF EVENTS
experiment
theory
Z_{b3} = 1-10
Z_{b3} = 11-20
Z_{b3} = 21-30
Z_{b3} = 31-40
Z_{b3} = 41-50
Z_{b3} = 51-60
Z_{b3} = 61-70
Z_{b3} = 71-80
A_{23}

Fig. 13